Geologica Acta, Vol.8, Nº 3, September 2010, 221-233
DOI: 10.1344/105.000001531
Available online at www.geologica-acta.com

geologica acta

Cement-rock interaction: Infiltration of a high-pH solution into a fractured granite core

JOSEP M. SOLER [1] **and URS K. MÄDER** [2]

[1] **Institute of Environmental Assessment and Water Research (IDAEA-CSIC)**
Jordi Girona 18-26, E-08034 Barcelona, Spain. E-mail: josep.soler@idaea.csic.es

[2] **Institute of Geological Sciences, University of Bern**
Baltzerstrasse 1-3, CH-3012 Bern, Switzerland. E-mail: urs@geo.unibe.ch

ABSTRACT

Within the framework of the HPF project (Hyperalkaline Plume in Fractured Rock) at the Grimsel Test Site (Switzerland), a small scale core infiltration experiment was performed at the University of Bern. A high-pH solution was continuously injected, under a constant pressure gradient, into a cylindrical core of granite containing a fracture. This high-pH solution was a synthetic version of solutions characteristic of early stages in the degradation of cement. The interaction between the rock and the solutions was reflected by significant changes in the composition of the injected solution, despite the negligible pH-buffering capacity, and a decrease in the permeability of the rock. Changes in the mineralogy and porosity of the fault gouge filling the fracture were only minor. Within the new LCS (Long-Term Cement Studies) project at Grimsel, new one-dimensional reactive transport modeling using CrunchFlow has been used to improve the interpretation of the experimental results. Dispersive and advective solute transport, adsorption processes and mineral reaction kinetics have been taken into account. The evolution of solution composition is mainly controlled by dissolution/precipitation reactions. Adsorption processes (cation exchange, surface complexation) only play a role in the very early stages of the experiment.

KEYWORDS | **Reactive transport modeling. Cement. Granite. Fracture. High-pH plume.**

INTRODUCTION

Cement is a major component of the engineered barrier system in proposed underground repositories for low- and intermediate-level radioactive waste. The interaction between groundwater and cement causes the generation of hyperalkaline solutions (pH 12.5 – 13.5), which may react with the rocks hosting the repositories and change their physical and chemical properties.

The evolution of the chemical composition of the solutions arising from the degradation of Ordinary Portland Cement in contact with groundwaters is characterized by the existence of 3 distinct phases (Berner, 1988, 1992). In the first stage, the solution composition is dominated by the dissolution of the alkali hydroxides in the cement, giving an initial pH of about 13.5. In the second stage, the pH is around 12.5 and is dominated by the dissolution of $Ca(OH)_2$. The third stage is characterized by the dissolution

of the C-S-H (calcium silicate hydrates) phases. Finally, phases other than C-S-H, such as hydrogarnet and ettringite are the ones that dissolve. The chemistry of the solution changes very significantly, with the pH going down to normal groundwater values, during the course of this final stage. The duration of these different stages depends on the amount of the cement in the repository and the flux of groundwater circulating through the system

The hyperalkaline solutions associated with the first two stages of degradation of the cement are chemically very aggressive (very far from equilibrium with respect to the minerals in the hosting rock formations) and may induce the dissolution and precipitation of different mineral phases. This alteration may also cause significant changes in the porosity and permeability of the rocks.

The HPF project at the Grimsel Test Site (Switzerland) addressed this issue in the context of a fractured crystalline host rock (granite). The granite and granodiorite at Grimsel are characterized by the presence of ductile shear zones (Bossart and Mazurek, 1991), with thicknesses ranging at least up to meter to decameter scales. These shear zones include mylonitic bands, which are bands of more intense deformation, with thicknesses up to several tens of centimeters. Brittle fractures developed in later stages of deformation, mainly in the mylonitic bands. These fractures, with thicknesses in the millimeter range, are at least partially filled with a highly porous fault gouge (crushed mylonite).

The HPF project, which was funded by ANDRA (France), JAEA (Japan), NAGRA (Switzerland), POSIVA (Finland), SKB (Sweden) and partly by DOE (USA), included an underground field experiment (injection of a hyperalkaline solution in a hydraulic dipole setting, tracer transport experiments), small-scale laboratory experiments, structural and mineralogical characterization, and flow and reactive transport modeling.

The results of a laboratory core-infiltration experiment were first interpreted by means of reactive transport modeling (Soler and Mäder 2007, 2005; Soler et al. 2006; Pfingsten et al., 2005). An important finding was that the interaction between the hyperalkaline solution and the fault gouge in the Grimsel granite caused a significant reduction in the hydraulic conductivity of the rock core, even though the amount of mineral alteration was minor. The arrival of the high-Ca front associated with the injected hyperalkaline solution was retarded (compared for instance with pH) due to its consumption by chemical reactions. The dissolution rates of primary minerals remained approximately constant during the experiment. However, the decrease in flow rate caused an overall displacement of the zone of secondary mineral precipitation (C-S-H/C-A-S-H) towards the inlet, which explained the increase in Si concentration at the outlet during the later stages of the experiment. Calcium concentrations decreased after the arrival of the high-Ca front due to increased net precipitation of C-S-H/C-A-S-H.

Although the main experimental trends were reproduced by the model, some discrepancies remained (e.g. retardation of the pH and Ca fronts at early stages, possibly caused by adsorption processes). In the framework of the new LCS project at Grimsel (Long-Term Cement Studies, funded by JAEA, NAGRA, NDA -Great Britain- and POSIVA), it was decided to perform a new modeling exercise to resolve these issues. This article describes the main experimental results and interpretation derived from a new reactive transport modeling exercise.

OVERVIEW OF THE EXPERIMENTAL METHODS

The interaction of a high pH-solution with the fractured Grimsel granite was investigated in laboratory (column) and field experiments. A complete description of the experiments can be found in Mäder et al. (2006).

In the small-scale laboratory experiment (Fig. 1), a high-pH (K-Na-Ca-OH) solution (ionic strength ≈ 0.2 mol/kg, pH = 13.36, T = 15ºC) was continuously injected, under a constant pressure gradient, into a cylindrical core of granite containing a fracture. The injected hyperalkaline solution was strongly undersaturated with respect to atmospheric CO_2. Any leakage of atmospheric CO_2 into the reservoir solution would have resulted in rapid precipitation of

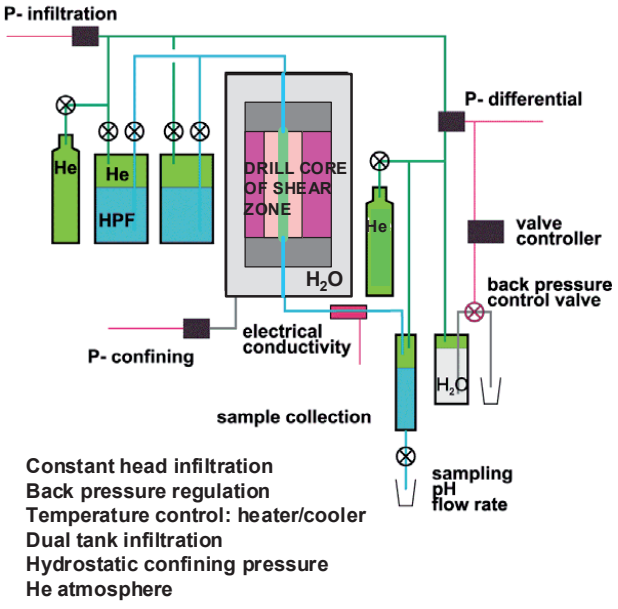

FIGURE 1 | **Schematic diagram showing the experimental setup for the core infiltration experiment.**

calcite. Therefore, pCO_2 was assumed to be at equilibrium with calcite defined by the Ca concentration and pH of the solution. The solution was collected at the opposite end of the core (outlet), after having circulated through the core. The length of the core was 7.8cm and its axis was oriented parallel to the fracture. Diameter was 5.9cm. The fracture was approximately planar, 5-10mm wide and filled by a fault gouge. The injection lasted 9 months. Before injecting high-pH solution, a tracer (NaCl) test had been performed with the core in order to estimate the porosity, dispersivity and hydraulic conductivity of the fracture.

The experimental results included the pH and concentrations of Al, Si and Ca at the outlet of the granite core. The pH did not seem to undergo a significant retardation or buffering with respect to the injected hydroxyl concentration. A decrease in fluid flow with time was observed, which indicated a decrease in hydraulic conductivity and implied an increasing water residence time within the sample. After the experiment, the observed amount of mineral alteration in the core was only minor and difficult to detect. The amounts were so small that it was not possible to fully characterize the secondary phases that precipitated except for a qualitative identification of a Ca-Si-hydrate phase (C-S-H).

This column experiment has been modeled by means of one-dimensional reactive transport simulations, taking into account advective-dispersive transport in a porous medium (fault gouge), chemical equilibria in solution (speciation), adsorption processes (cation exchange, surface complexation), and mineral reactions described by kinetic rate laws. Unlike previous modeling, the time-dependent flow has been fixed in the model (independent of mineralogical alteration) to focus on the geochemical behavior of the system.

DESCRIPTION OF THE REACTIVE TRANSPORT CODE

Reactive transport modeling was performed using CrunchFlow (Steefel, 2008). Details of the code can be found in the user's manual (downloadable from www.csteefel.com). Only an outline will be given here.

Crunchflow solves numerically the advection-dispersion-reaction equations

$$\frac{\partial(\phi(C_i^{mob}+C_i^{immob}))}{\partial t}=\nabla\cdot\left(D\nabla C_i^{mob}\right)-\nabla\cdot\left(qC_i^{mob}\right)+R_i \qquad (i=1,2,\ldots,N_{tot}) \tag{1}$$

where ϕ is porosity, C_i^{mob} is the concentration of mobile species i in solution, C_i^{immob} is the concentration of immobile species i in solution (sorbed by surface complexation or ion exchange), D is the combined dispersion-diffusion coefficient, q is Darcy velocity, R_i is the total reaction rate affecting species i, t is time and N_{tot} is the total number of aqueous species. The total reaction rate for species i, R_i, is given by

$$R_i=-\sum_m \nu_{im}R_m \tag{2}$$

where R_m is the rate of precipitation ($R_m>0$) or dissolution ($R_m<0$) of mineral m per unit volume of rock, and v_{in} is the number of moles of i per mole of mineral m.

Since mineral reactions are described using kinetic rate laws, initial mineral surface areas and several reaction rate parameters have to be supplied by the user as input. In this set of simulations, the reaction rate laws that have been used are of the form

$$R_m=\mathrm{sgn}\left(\log\frac{IAP}{K_{eq}}\right)A_m k_m a_{H^+}^n f_m(\Delta G) \tag{3}$$

where R_m is the reaction rate for a given mineral in units of mol/m^{3}rock/s, A_m is the mineral surface area (m^2/m^{3}rock), k_m is the reaction rate constant (mol/m^2/s) at the temperature of interest, $a_{H^+}^n$ is the term describing the effect of pH on the rate, and $f_m(\Delta G)$ is the function describing the dependence of the rate on solution saturation state. The $f_m(\Delta G)$ function has the form

$$f_m(\Delta G)=\left|\exp\left(\frac{\Delta G}{RT}\right)-1\right|=\left|\frac{IAP}{K_{eq}}-1\right| \tag{4}$$

where ΔG is the Gibbs energy of the reaction (J/mol), R is the gas constant, T is temperature (K), IAP is the ionic activity product of the solution with respect to the mineral, and K_{eq} is the equilibrium constant for that mineral reaction (ionic activity product at equilibrium). The sgn term in Eq. (3) gives the sign of the expression; rates are negative for dissolution and positive for precipitation.

Changes in mineral surface area A (m^2/m^{3}bulk) due to reaction are calculated according to

$$A=A^{initial}\left(\phi_m/\phi_m^{initial}\right)^{2/3}\left(\phi/\phi^{initial}\right)^{2/3} \qquad \text{(dissolution)} \tag{5}$$

$$A=A^{initial}\left(\phi/\phi^{initial}\right)^{2/3} \qquad \text{(precipitation)} \tag{6}$$

The inclusion of a 2/3 dependence on porosity is chiefly to ensure that as the porosity goes to 0, so too does the mineral surface area available for reaction. This formulation is used primarily for primary minerals (that is, minerals with initial volume fractions > 0). For secondary minerals which precipitate, the value of the initial bulk surface area specified is used as long as precipitation occurs. If this

phase later dissolves, the above formulation is used, but with an arbitrary "initial volume fraction" of 0.01.

MODEL PARAMETERS

Dimensions

The length of the one-dimensional domain was 7.8cm (the length of the core). Grid spacing was 1mm, although a finer discretization was used near the inlet (0.25mm in the first mm of the domain). This discretization proved to be sufficient to obtain good numerical convergence in previous modeling of the experiment (Soler and Mäder, 2007), which also included coupling of flow and mineralogy changes.

Rock composition

The initial mineralogical composition and porosity of the rock (fault gouge filling the fracture) used in the model is given in Table 1. The porosity was determined through the interpretation of a NaCl tracer test performed before the injection of the high-pH solution (Soler and Mäder, 2007; Soler et al., 2006).

The surface areas of the primary minerals were the main parameters that were fitted to adjust the model to the experimental results. Surface areas are proportional to the relative volume fractions (except for the small fraction of fine-grained albite). Regarding the secondary minerals, an initial surface area equal to $10000 m^2/m^3$ is assumed when a secondary mineral starts precipitating. This large surface area, together with the large rate constants, leads to fast precipitation/dissolution, i.e. conditions very close to local equilibrium with respect to these phases. The potential secondary minerals that were taken into account in the calculations are given in Table 2. The composition and crystallinity of the secondary minerals that actually precipitated in the experiment could not be determined due to the small amounts present.

TABLE 1 | **Initial mineralogical composition. Additionally, a small volume fraction of albite (0.03%) with a very large surface area ($3x10^5 m^2/m^3$) was included, to simulate the initial peaks in Al and Si concentrations at breakthrough.**

Mineral	Volume fraction (%)	Surface area (m^2/m^3)
Quartz	19	10730
Albite	14	7920
Microcline	15	8480
Phlogopite	09	5100
Muscovite	22	12420
Porosity	21	-

TABLE 2 | **Potential secondary phases included in the model. C-S-H ss refers to discrete phases defined from the cementitious C-S-H solid solution model by Kulik and Kersten (2001).**

Calcite	$CaCO_3$
Portlandite	$Ca(OH)_2$
Brucite	$Mg(OH)_2$
C-S-H-1667	C-S-H ss, Ca/Si=1.67
C-S-H-14	C-S-H ss, Ca/Si=1.4
C-S-H-12	C-S-H ss, Ca/Si=1.2
C-S-H-10	C-S-H ss, Ca/Si=1.0
C-S-H-08	C-S-H ss, Ca/Si=0.8
C-S-H-06	C-S-H ss, Ca/Si=0.6
C-S-H-04	C-S-H ss, Ca/Si=0.4
C-S-H-02	C-S-H ss, Ca/Si=0.2
C-S-H-00	C-S-H ss, Ca/Si=0.0
Analcime	Na-zeolite
Laumontite	Ca-zeolite
Mesolite	Na-Ca-zeolite
Natrolite	Na-zeolite
Scolecite	Ca-zeolite
Stilbite	Na-Ca-zeolite
Gismondine	Ca-zeolite
Mordenite	Na-Ca-zeolite
Wairakite	Ca-zeolite
Prehnite	$Ca_2Al_2Si_3O_{10}(OH)_2$
Foshagite	C-S-H phase, Ca/Si=1.33
Gyrolite	C-S-H phase, Ca/Si=0.66
Hillebrandite	C-S-H phase, Ca/Si=2.0
Okenite	C-S-H phase, Ca/Si=0.5
Tobermorite-14A	C-S-H phase, Ca/Si=0.83

Solution composition

The composition of the high-pH solution injected into the granite core and the initial composition of the water in the pores of the fault gouge is given in Table 3. The composition of the high-pH solution would correspond to an early stage in the degradation of cement in contact with Grimsel groundwater. This solution is at equilibrium with portlandite and calcite and undersaturated with respect to all the primary minerals, except for phlogopite (slightly supersaturated). The calculated pH (13.47) is slightly larger than the measured pH (13.36). The initial

TABLE 3 | **Composition (total molalities, pH and T) of the high-pH solution entering the domain and the initial fluid in the pores of the rock. pH of the high-pH solution and Ca concentration of the initial solution are calculated by charge balance.**

	High-pH solution	Initial solution
T (°C)	15	15
pH	13.47	9.0
Al	$9.1x10^{-9}$	$5.6x10^{-7}$
SiO_2	$3.9x10^{-6}$	$2.4x10^{-4}$
Na	$6.5x10^{-2}$	$6.7x10^{-4}$
K	$1.3x10^{-1}$	$3.8x10^{-6}$
Ca	$2.1x10^{-3}$	$2.5x10^{-4}$
Mg	$6.7x10^{-9}$	$4.1x10^{-7}$
CO_3	$6.2x10^{-5}$	$5.5x10^{-4}$
SO_4	$9.3x10^{-7}$	$5.7x10^{-5}$
Cl	$2.4x10^{-6}$	$1.5x10^{-4}$
F	$5.1x10^{-6}$	$3.1x10^{-4}$

composition corresponds to Grimsel groundwater (Mäder et al., 2006; Eikenberg et al., 1994) and is at equilibrium with calcite. pH has been fixed to 9 (instead of 9.6 at Grimsel) to match the early pH breakthrough in the experiment. Uncertainties in this initial composition are not very important, because the initial fluid is flushed out of the rock very quickly.

Thermodynamic data

Thirty-two minerals (35 when including trace minerals) and 43 species in solution have been taken into account in the calculations. All the chemical equilibria in solution are listed in Table 4. The equilibrium constants for all the mineral reactions are given in Table 5. All the equilibrium constants at 15°C were taken from the database included in CrunchFlow, which is based on the EQ3/6 database (Wolery et al., 1990), except for the C-S-H ss phases (calculated from the data in Kulik and Kersten, 2001) and montmorillonite (Marty et al., 2009). Activity coefficients are calculated using the extended Debye-Hückel formulation (b-dot model), with parameters from the same database. The activity of water is taken to be unity.

Reaction rates

Table 6 shows the rate parameters used for the primary minerals. These rates are calculated from the data in the compilation by Rochelle and Noy (2000), also reported in Soler et al. (2006). Regarding the secondary minerals, large reaction rate constants have been applied (k_m=10^{-9} mol/m²/s;

TABLE 4 | **Equilibrium constants (log K_{eq}) and stoichiometric coefficients for equilibria in solution. Reactions are written as the destruction of 1 mole of the species in the first column.**

Species	log K	Stoichiometric Coefficients										
		Al^{+++}	$SiO_{2(aq)}$	Na^+	K^+	Ca^{++}	Mg^{++}	HCO_3^-	SO_4^{--}	H^+	Cl^-	F^-
$Al(OH)_2^+$	1.1187E+01	1.00	0.00	0.00	0.00	0.00	0.00	0.00	0.00	-2.00	0.00	0.00
AlO_2^-	2.3980E+01	1.00	0.00	0.00	0.00	0.00	0.00	0.00	0.00	-4.00	0.00	0.00
$AlOH^{++}$	5.2549E+00	1.00	0.00	0.00	0.00	0.00	0.00	0.00	0.00	-1.00	0.00	0.00
$CO_{2(aq)}$	-6.4124E+00	0.00	0.00	0.00	0.00	0.00	0.00	1.00	0.00	1.00	0.00	0.00
CO_3^{--}	1.0423E+01	0.00	0.00	0.00	0.00	0.00	0.00	1.00	0.00	-1.00	0.00	0.00
$CaCO_{3(aq)}$	7.1962E+00	0.00	0.00	0.00	0.00	1.00	0.00	1.00	0.00	-1.00	0.00	0.00
$CaCl^+$	7.0439E-01	0.00	0.00	0.00	0.00	1.00	0.00	0.00	0.00	0.00	1.00	0.00
$CaCl_{2(aq)}$	6.0320E-01	0.00	0.00	0.00	0.00	1.00	0.00	0.00	0.00	0.00	2.00	0.00
CaF^+	-6.5260E-01	0.00	0.00	0.00	0.00	1.00	0.00	0.00	0.00	0.00	0.00	1.00
$CaHCO_3^+$	-1.0448E+00	0.00	0.00	0.00	0.00	1.00	0.00	1.00	0.00	0.00	0.00	0.00
$CaOH^+$	1.2850E+01	0.00	0.00	0.00	0.00	1.00	0.00	0.00	0.00	-1.00	0.00	0.00
$CaSO_{4(aq)}$	-2.0746E+00	0.00	0.00	0.00	0.00	1.00	0.00	0.00	1.00	0.00	0.00	0.00
$H_2SiO_4^{--}$	2.2960E+01	0.00	1.00	0.00	0.00	0.00	0.00	0.00	0.00	-2.00	0.00	0.00
$HAlO_{2(aq)}$	1.7305E+01	1.00	0.00	0.00	0.00	0.00	0.00	0.00	0.00	-3.00	0.00	0.00
$HSiO_3^-$	1.0093E+01	0.00	1.00	0.00	0.00	0.00	0.00	0.00	0.00	-1.00	0.00	0.00
$KCl_{(aq)}$	1.5848E+00	0.00	0.00	0.00	1.00	0.00	0.00	0.00	0.00	0.00	1.00	0.00
$KOH_{(aq)}$	1.4460E+01	0.00	0.00	0.00	1.00	0.00	0.00	0.00	0.00	-1.00	0.00	0.00
KSO_4^-	-8.6532E-01	0.00	0.00	0.00	1.00	0.00	0.00	0.00	1.00	0.00	0.00	0.00
$MgCO_{3(aq)}$	7.5022E+00	0.00	0.00	0.00	0.00	0.00	1.00	1.00	0.00	-1.00	0.00	0.00
$MgCl^+$	1.2368E-01	0.00	0.00	0.00	0.00	0.00	1.00	0.00	0.00	0.00	1.00	0.00
MgF^+	-1.3452E+00	0.00	0.00	0.00	0.00	0.00	1.00	0.00	0.00	0.00	0.00	1.00
$MgHCO_3^+$	-1.0317E+00	0.00	0.00	0.00	0.00	0.00	1.00	1.00	0.00	0.00	0.00	0.00
$MgSO_{4(aq)}$	-2.2981E+00	0.00	0.00	0.00	0.00	0.00	1.00	0.00	1.00	0.00	0.00	0.00
$NaAlO_{2(aq)}$	2.4779E+01	1.00	0.00	1.00	0.00	0.00	0.00	0.00	0.00	-4.00	0.00	0.00
$NaCO_3^-$	9.7931E+00	0.00	0.00	1.00	0.00	0.00	0.00	1.00	0.00	-1.00	0.00	0.00
$NaCl_{(aq)}$	8.0833E-01	0.00	0.00	1.00	0.00	0.00	0.00	0.00	0.00	0.00	1.00	0.00
$NaF_{(aq)}$	1.0414E+00	0.00	0.00	1.00	0.00	0.00	0.00	0.00	0.00	0.00	0.00	1.00
$NaHCO_{3(aq)}$	-2.3870E-01	0.00	0.00	1.00	0.00	0.00	0.00	1.00	0.00	0.00	0.00	0.00
$NaHSiO_{3(aq)}$	8.3570E+00	0.00	1.00	1.00	0.00	0.00	0.00	0.00	0.00	-1.00	0.00	0.00
$NaOH_{(aq)}$	1.5123E+01	0.00	0.00	1.00	0.00	0.00	0.00	0.00	0.00	-1.00	0.00	0.00
$NaSO_4^-$	-8.2000E-01	0.00	0.00	1.00	0.00	0.00	0.00	0.00	1.00	0.00	0.00	0.00
OH^-	1.4338E+01	0.00	0.00	0.00	0.00	0.00	0.00	0.00	0.00	-1.00	0.00	0.00

TABLE 5 | **Equilibrium constants for the mineral reactions, written as the dissolution of 1 mole of mineral. The possible secondary phases include phases usually associated with the alteration caused by hyperalkaline solutions. Data for trace minerals (clinozoisite, montmorillonite, clinochlore) are also included.**

Mineral	log K	Stoichiometric Coefficients										
		Al^{+++}	SiO_{2aq}	Na^{+}	K^{+}	Ca^{++}	Mg^{++}	HCO_3^{-}	SO_4^{--}	H^{+}	Cl^{-}	F^{-}
Quartz	-4.2222E+00	0.00	1.00	0.00	0.00	0.00	0.00	0.00	0.00	0.00	0.00	0.00
Albite	3.0108E+00	1.00	3.00	1.00	0.00	0.00	0.00	0.00	0.00	-4.00	0.00	0.00
Albite2	3.0108E+00	1.00	3.00	1.00	0.00	0.00	0.00	0.00	0.00	-4.00	0.00	0.00
Microcline	-2.0041E-01	1.00	3.00	0.00	1.00	0.00	0.00	0.00	0.00	-4.00	0.00	0.00
Phlogopite	3.9259E+01	1.00	3.00	0.00	1.00	0.00	3.00	0.00	0.00	-10.00	0.00	0.00
Muscovite	1.4990E+01	3.00	3.00	0.00	1.00	0.00	0.00	0.00	0.00	-10.00	0.00	0.00
Calcite	2.0050E+00	0.00	0.00	0.00	0.00	1.00	0.00	1.00	0.00	-1.00	0.00	0.00
Portlandite	2.3340E+01	0.00	0.00	0.00	0.00	1.00	0.00	0.00	0.00	-2.00	0.00	0.00
Brucite	1.6976E+01	0.00	0.00	0.00	0.00	0.00	1.00	0.00	0.00	-2.00	0.00	0.00
CSH-1667	3.0164E+01	0.00	1.00	0.00	0.00	1.67	0.00	0.00	0.00	-3.34	0.00	0.00
CSH-14	2.3942E+01	0.00	1.00	0.00	0.00	1.40	0.00	0.00	0.00	-2.80	0.00	0.00
CSH-12	1.9458E+01	0.00	1.00	0.00	0.00	1.20	0.00	0.00	0.00	-2.40	0.00	0.00
CSH-10	1.5080E+01	0.00	1.00	0.00	0.00	1.00	0.00	0.00	0.00	-2.00	0.00	0.00
CSH-08	2.5433E+01	0.00	2.27	0.00	0.00	1.82	0.00	0.00	0.00	-3.64	0.00	0.00
CSH-06	1.3710E+01	0.00	1.72	0.00	0.00	1.03	0.00	0.00	0.00	-2.06	0.00	0.00
CSH-04	6.6928E+00	0.00	1.39	0.00	0.00	0.56	0.00	0.00	0.00	-1.12	0.00	0.00
CSH-02	2.0311E+00	0.00	1.16	0.00	0.00	0.23	0.00	0.00	0.00	-0.46	0.00	0.00
CSH-00	-1.2416E+00	0.00	1.00	0.00	0.00	0.00	0.00	0.00	0.00	0.00	0.00	0.00
Analcime	6.5548E+00	0.96	2.04	0.96	0.00	0.00	0.00	0.00	0.00	-3.84	0.00	0.00
Laumontite	1.4698E+01	2.00	4.00	0.00	0.00	1.00	0.00	0.00	0.00	-8.00	0.00	0.00
Mesolite	1.4645E+01	1.99	3.01	0.68	0.00	0.66	0.00	0.00	0.00	-7.96	0.00	0.00
Natrolite	1.9590E+01	2.00	3.00	2.00	0.00	0.00	0.00	0.00	0.00	-8.00	0.00	0.00
Scolecite	1.7055E+01	2.00	3.00	0.00	0.00	1.00	0.00	0.00	0.00	-8.00	0.00	0.00
Stilbite	1.4087E+00	2.18	6.82	0.14	0.01	1.02	0.00	0.00	0.00	-8.72	0.00	0.00
Gismondine	4.1717E+01	4.00	4.00	0.00	0.00	2.00	0.00	0.00	0.00	-16.00	0.00	0.00
Mordenite	-5.4107E+00	0.94	5.06	0.36	0.00	0.29	0.00	0.00	0.00	-3.76	0.00	0.00
Wairakite	1.9428E+01	2.00	4.00	0.00	0.00	1.00	0.00	0.00	0.00	-8.00	0.00	0.00
Prehnite	3.4756E+01	2.00	3.00	0.00	0.00	2.00	0.00	0.00	0.00	-10.00	0.00	0.00
Foshagite	6.8048E+01	0.00	3.00	0.00	0.00	4.00	0.00	0.00	0.00	-8.00	0.00	0.00
Gyrolite	2.3353E+01	0.00	3.00	0.00	0.00	2.00	0.00	0.00	0.00	-4.00	0.00	0.00
Hillebrandite	3.8035E+01	0.00	1.00	0.00	0.00	2.00	0.00	0.00	0.00	-4.00	0.00	0.00
Okenite	1.0464E+01	0.00	2.00	0.00	0.00	1.00	0.00	0.00	0.00	-2.00	0.00	0.00
Tobermorite	6.5137E+01	0.00	6.00	0.00	0.00	5.00	0.00	0.00	0.00	-10.00	0.00	0.00
Clinozoisite	4.5966E+01	3.00	3.00	0.00	0.00	2.00	0.00	0.00	0.00	-13.00	0.00	0.00
Montmorillon.	1.3405E+01	3.32	8.00	0.68	0.00	0.00	0.68	0.00	0.00	-11.80	0.00	0.20
Clinochlore	-7.0894E+01	2.00	3.00	0.00	0.00	0.00	5.00	0.00	0.00	-16.00	0.00	0.00

k_m=10^{-8} mol/m²/s for calcite) to simulate local equilibrium for the precipitation of secondary phases.

Cation exchange - surface complexation

Cation exchange capacity and cation occupancies on the fault gouge filling the fracture have been measured (Mazurek, 2003; Mäder & Ekberg, 2006). Cation exchange has been included in the model, according to the reactions below (Gaines-Thomas convention). The log K values have been fitted to match the measured occupancies (76% Ca, 15% K, 5% Na, 4% Mg with Grimsel groundwater; 83% Ca, 12% K, 3% Na, 2% Mg with the initial water in the model). CEC is 11.1 meq/kg.

TABLE 6 | **Rate parameters for the primary minerals (see Eq. 3). Parameters are calculated from the data in Rochelle and Noy (2000), except for montmorillonite (Marty et al., 2009).**

Mineral m	log k_m (mol/m²/s)	n $\left(a^{n}_{H^+}\right)$
Quartz	-13.92	-0.2
Albite	-12.92	-0.2
Microcline	-20.22	-0.73
Phlogopite	-13.52	-0.2
Muscovite	-13.12	-0.1
Clinozoisite	-13.92	-0.2
Montmorillonite	-16.46	-0.34
Clinochlore	-14.60	-0.2

$$\equiv K \Leftrightarrow K^{+} + \equiv \qquad \log K = -2.7 \tag{7}$$

$$\equiv Na \Leftrightarrow Na^{+} + \equiv \qquad \log K = 0.1 \tag{8}$$

$$\equiv Ca \Leftrightarrow Ca^{2+} + 2 \equiv \qquad \log K = 0.0 \tag{9}$$

$$\equiv Mg \Leftrightarrow Mg^{2+} + 2 \equiv \qquad \log K = -1.2 \tag{10}$$

Surface complexation (no electrostatic correction, surface concentrations in mol/kg_H_2O) has also been included in the model, as two different sites on the muscovite surface. The reaction on one site is given by

$$> OCa^{+} + 2H^{+} \Leftrightarrow > OH_2^{+} + Ca^{2+} \quad \log K = 6.2,\ 0.001 \text{ sites/m}^2 \tag{11}$$

The log K and the number of sites have been fitted to match the observed pH (and also Ca) breakthroughs. On the second site (0.005 sites/m^2), the reactions are

$$>O^- + H^+ \Leftrightarrow >OH \qquad \log K = 6.2 \qquad (12)$$

$$>OH_2^+ \Leftrightarrow >OH + H^+ \qquad \log K = -5.5 \qquad (13)$$

The log K values have been taken from Bradbury et al. (2005) for strong sites on illite. The number of sites has been adjusted to refine pH breakthrough (the effect is small; see below).

Flow and transport parameters

Before injecting high-pH solution, a tracer (NaCl) test was performed in order to estimate the porosity and dispersivity of the fracture. The results were successfully analyzed by fitting the analytical solution of the one-dimensional advection-dispersion equation to the observed breakthrough curve (Soler and Mäder, 2007; Soler et al., 2006). The results of the test provided the following parameter values: Porosity $\phi = 0.21$, dispersivity $\alpha = 0.014$m. Effective diffusion coefficient was calculated according to Archie´s law ($D_e = \phi^2 D_0$) with $D_0 = 10^{-9}$m^2/s. The combined dispersion-diffusion coefficient D was always dominated by dispersion.

Flow velocity through the core changed during the infiltration of high-pH solution, due to changes in permeability. In previous modeling of the experiment (Soler and Mäder, 2007; Soler et al., 2006), changes in fluid flow were coupled to porosity and mineralogy changes. In this study, it was decided to use a fixed time-dependent flow (Fig.2; not coupled to reaction), to be able to focus on geochemical behavior.

RESULTS

Results will be shown first for a reference case, followed by the results of a sensitivity study with respect to different parameters.

Reference case

Figure 3 shows the evolution of solution composition at breakthrough. The initial peak in Si and Al concentrations is caused by the dissolution of fines (fine-grained albite in the model). The arrival of the Ca concentration front is retarded by precipitation of secondary phases (C-S-H) and uptake at surface complexation sites. The increase in Si concentration at later stages is caused by the increasing residence time of the solution in the core (decreasing flow velocity), which cannot be balanced by the precipitation of secondary phases. Figure 4 shows the evolution of pH at breakthrough. There is a slight retardation of the high-pH front mostly controlled by surface complexation (uptake of Ca^{2+} and release of H^+). In order to obtain a reasonable fit between model and experimental results, total mineral surface areas about 3.4x10^{5}m^2/m^3 had to be used. Specific surface areas measured by BET (0.5 to 8m^2/g) translated into values ranging from 5x10^6 to 8x10^{7}m^2/m^3. Surface area in the model is dominated by the fine-grained fraction (see Table 1).

Figure 5 shows the calculated mineral content along the fracture at the end of the experiment. Primary minerals remain largely unaltered and the amounts of secondary phases are very small, which is consistent with the experimental observations.

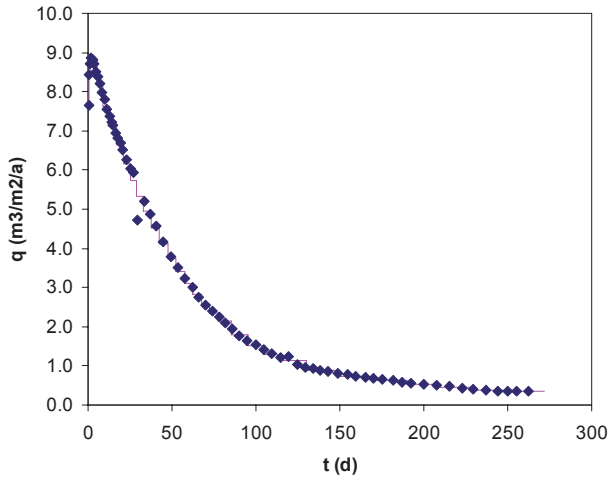

FIGURE 2 | **Darcy velocity along the fracture (m^3/m^2/a) vs. time. Symbols correspond to experimental masurements; line corresponds to values used in the model (constant velocity during multiple short time intervals).**

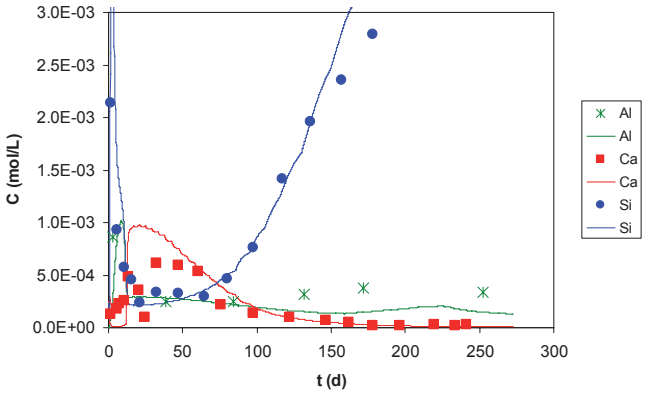

FIGURE 3 | **Change in the composition of the solution at the outlet of the experiment. Symbols correspond to experimental data and lines to model results.**

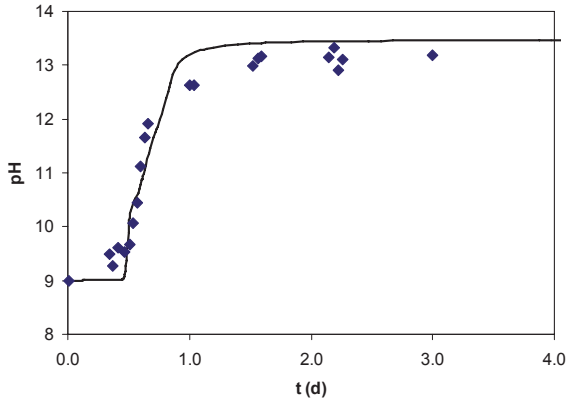

FIGURE 4 | **pH vs. time (early pH breakthrough). Symbols correspond to experimental data and lines to model results.**

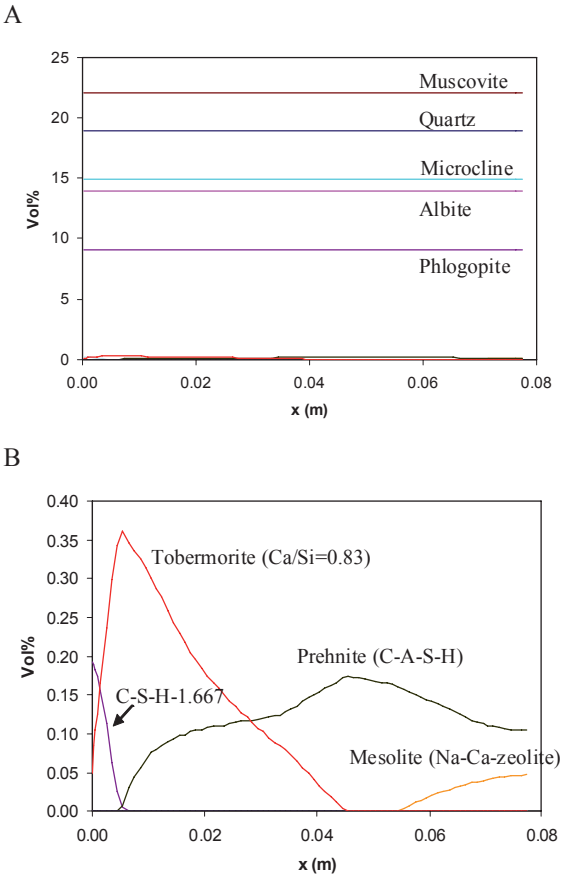

FIGURE 5 | **Calculated A) primary and B) secondary mineral contents along the fracture at the end of the experiment.**

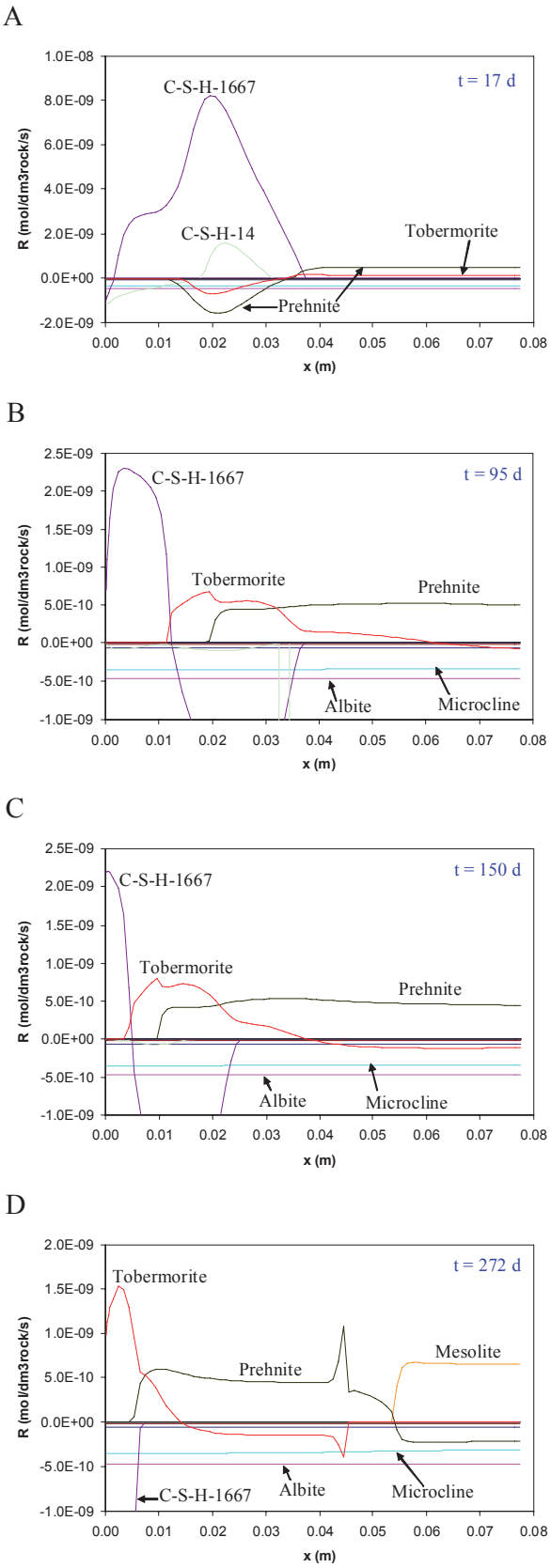

FIGURE 6 | **Reaction rates vs. distance at 4 different times (17, 95, 150, 272 d). Negative rates mean dissolution; positive rates mean precipitation.**

Figure 6 shows reaction rates along the fracture at 4 different times (17, 95, 150 and 272 d). Albite and microcline dissolve always under far-from-equilibrium conditions. Quartz and muscovite also dissolve, but the magnitudes of the rates are much smaller. Phlogopite undergoes very little reaction. Regarding the secondary phases, at early times there is precipitation of C-S-H ss (Ca/Si = 1.67) followed by a zone with tobermorite (crystalline C-S-H, Ca/Si = 0.83) and prehnite (here an analogue of a C-A-S-H phase). With time and increasing solution residence time in the core (decreasing flow velocity), tobermorite replaces C-S-H ss, prehnite replaces tobermorite, and eventually mesolite (Na-Ca-zeolite) replaces prehnite. A series of reaction fronts develop and propagate in the upstream direction (from right to left in the plots).

Case without cation exchange - Ca surface complexation

In this case Eqs. 7 to 11 were not included in the model. The biggest differences with respect to the reference case are the lack of retardation for the pH, K and Na fronts (Figs. 7, 8) and the smaller retardation for the arrival of the Ca front (Fig. 9).

Case without protonation-deprotonation

In this case Eqs. 12 and 13 were not included in the model. The only significant difference with respect to the reference case is in the very early breakthrough of the high-pH front (Fig. 10).

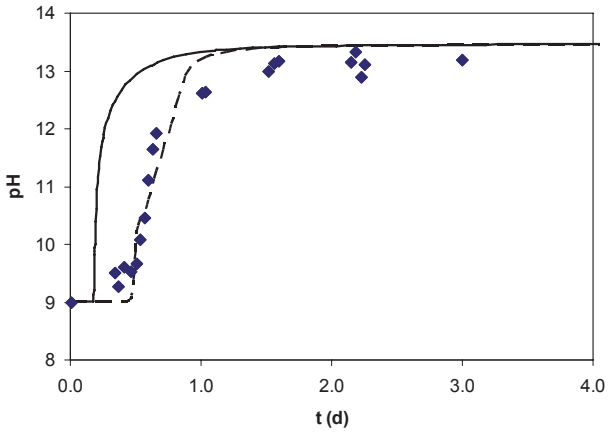

FIGURE 7 | **pH vs. time (early pH breakthrough) for the reference case (dashed line) and the case without cation exchange and Ca surface complexation (solid line). Symbols correspond to experimental data and lines to model results.**

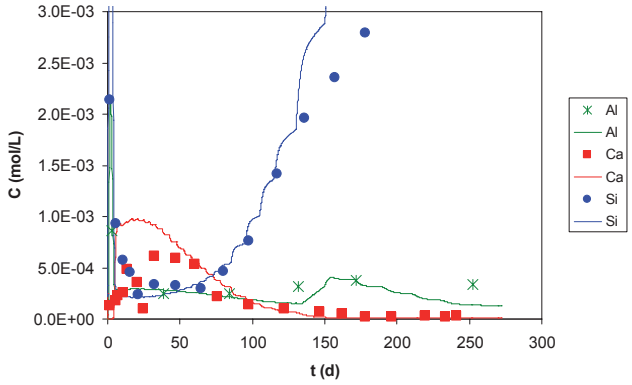

FIGURE 9 | **Change in the composition of the solution at the outlet of the experiment for the case without cation exchange and Ca surface complexation (solid line). Symbols correspond to experimental data and lines to model results. The jagged appearance of the curves is due to the step-like evolution of flow velocities imposed in the model. Notice the earlier breakthrough of Ca, compared to Fig. 3.**

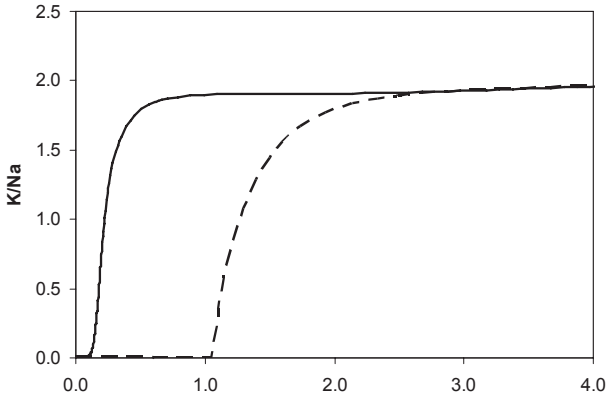

FIGURE 8 | **K/Na atomic ratio in solution vs. time (early pH breakthrough) for the reference case (dashed line) and the case without cation exchange and Ca surface complexation (solid line).**

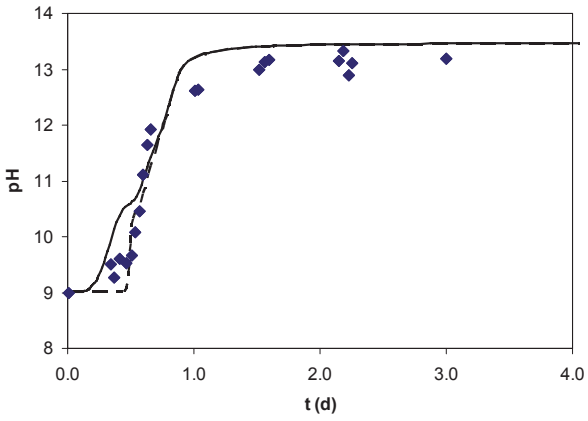

FIGURE 10 | **pH vs. time (early pH breakthrough) for the reference case (dashed line) and the case without protonation-deprotonation (solid line). Symbols correspond to experimental data and lines to model results.**

Case without zeolites

In this case zeolites were not allowed to precipitate as potential secondary minerals. No major differences regarding solution chemistry were observed (Fig. 11).

Case without crystalline C-S-H phases

In this case crystalline C-S-H phases (e.g. tobermorite) were not allowed to precipitate as potential secondary minerals. However, cementitious C-S-H phases (solid solution) were allowed to precipitate. The main difference regarding solution chemistry with respect to the reference case is the overestimation of Si concentration in solution (Fig. 12a). Instead of tobermorite, cementitious C-S-H with Ca/Si ratios lower than 1.667 precipitate in the fracture (Fig. 12c).

Case without prehnite

In this case prehnite, used here as an analogue of a C-A-S-H phase, was not allowed to precipitate.

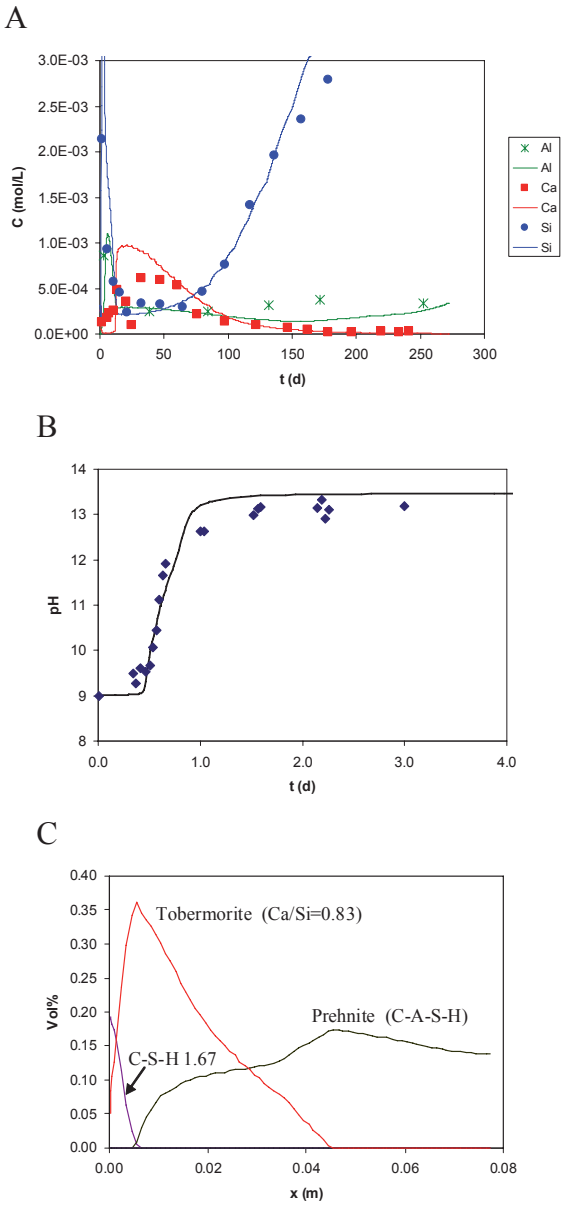

FIGURE 11 | **From top to bottom: A) Change in the composition of the solution at the outlet of the experiment for the case without zeolite precipitation. B) pH vs. time (early pH breakthrough). C) Calculated secondary mineral contents along the fracture at the end of the experiment. Symbols correspond to experimental data and lines to model results.**

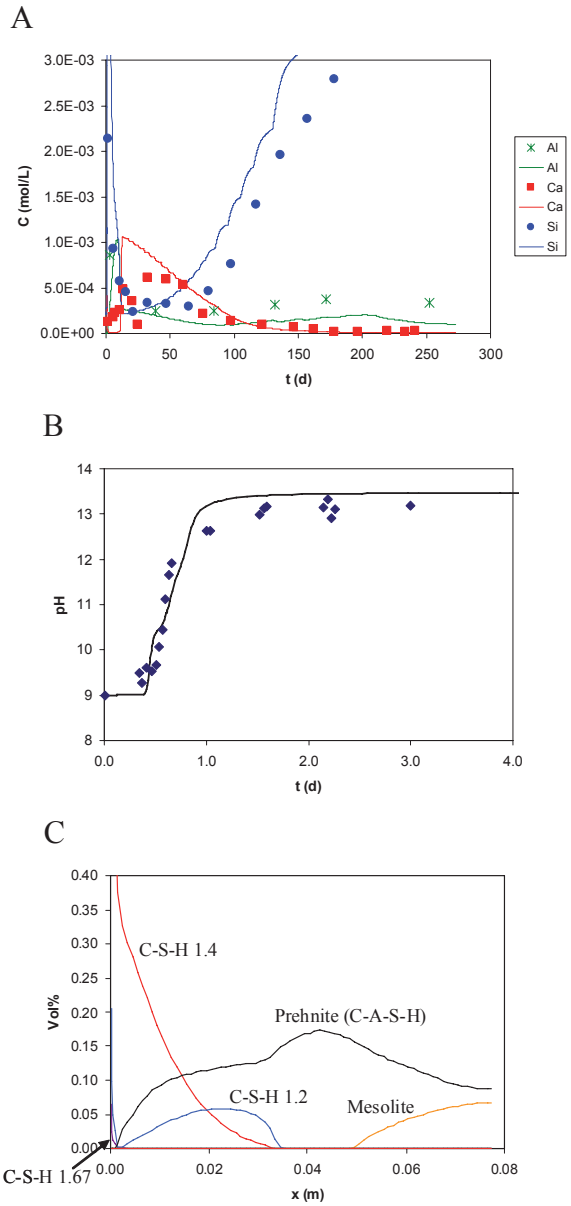

FIGURE 12 | **From top to bottom: A) Change in the composition of the solution at the outlet of the experiment for the case without crystalline C-S-H phases. B) pH vs. time (early pH breakthrough). C) Calculated secondary mineral contents along the fracture at the end of the experiment. Symbols correspond to experimental data and lines to model results.**

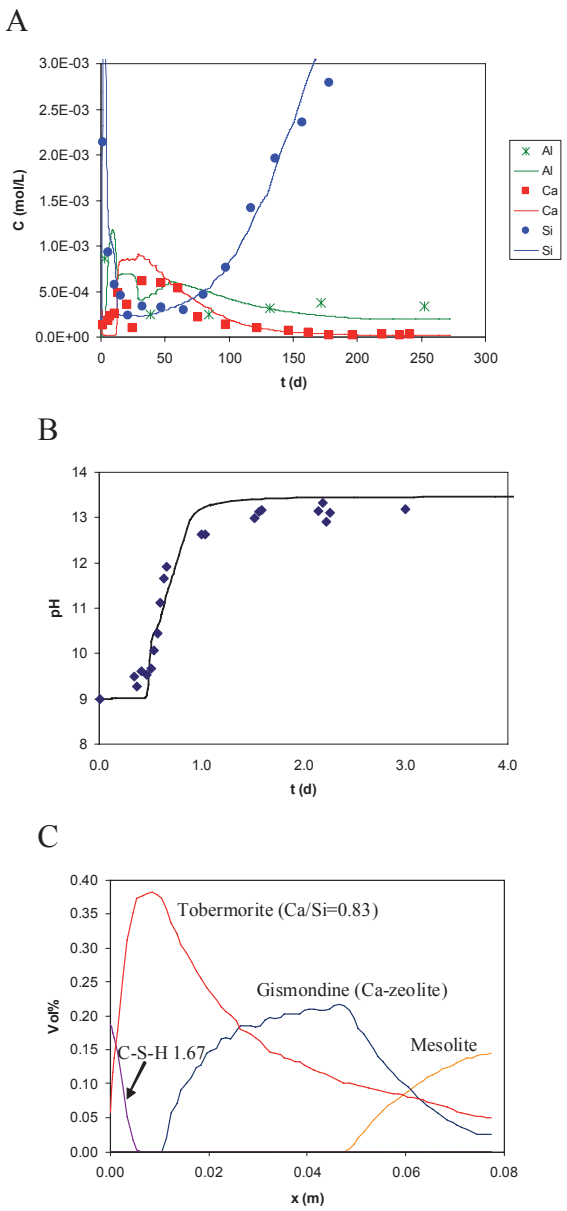

FIGURE 13 | **From top to bottom: A) Change in the composition of the solution at the outlet of the experiment for the case without prehnite. B) pH vs. time (early pH breakthrough). C) Calculated secondary mineral contents along the fracture at the end of the experiment. Symbols correspond to experimental data and lines to model results.**

The result is that a Ca-zeolite (gismondine) precipitates instead. No major changes are observed in the calculated solution chemistry (Fig. 13), except for the stabilization of Si concentration at late stages (t > 210 d; not shown) due to the replacement of gismondine (Ca-zeolite) by mesolite (Ca-Na-zeolite) in the fracture, together with the dissolution of albite and microcline.

Case including trace primary minerals

In this case small amounts of trace primary minerals were included in the model (Table 7), to check the potential effect of these phases in the results. These trace minerals are clinozoisite (Al end-member for epidote), a Na-montmorillonite and clinochlore (Mg-end member for chlorite). Surface areas were assigned according to the same area/volume_fraction ratio as for the other primary minerals. No significant changes in the results were observed (Fig. 14), due to the negligible reaction of these trace minerals.

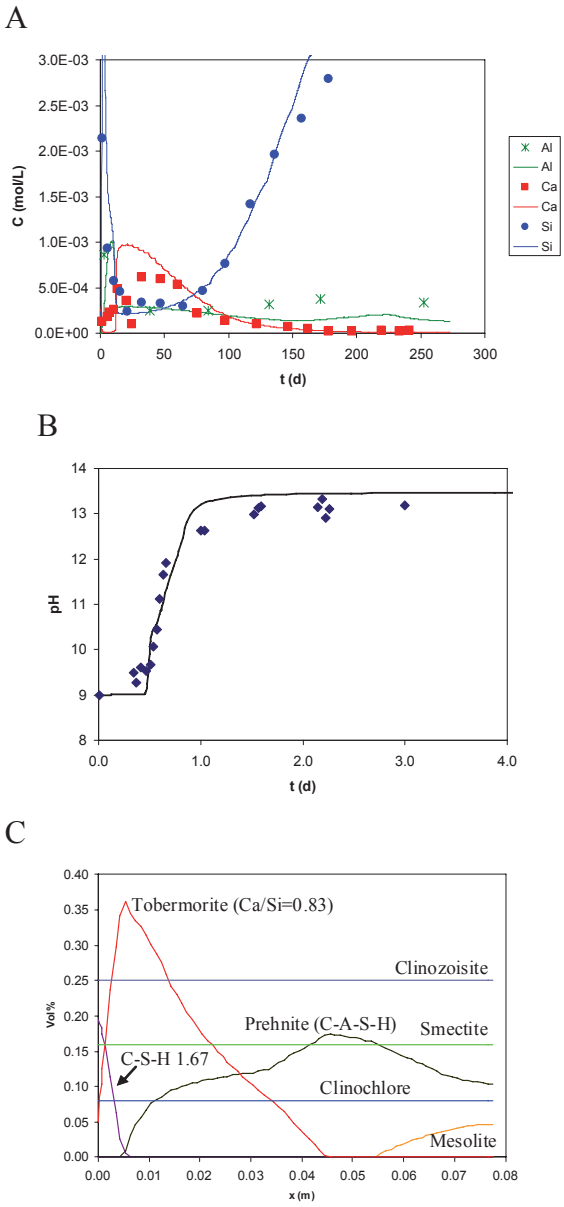

FIGURE 14 | **From top to bottom: A) Change in the composition of the solution at the outlet of the experiment for the case including trace primary minerals. B) pH vs. time (early pH breakthrough). C) Calculated secondary and trace primary mineral contents along the fracture at the end of the experiment. Symbols correspond to experimental data and lines to model results.**

TABLE 7 | **Initial mineralogical composition for the case including trace minerals. Additionally, a small volume fraction of albite (0.03%) with a very large surface area (3x105m2/m3) was included, to simulate the initial peaks in Al and Si concentrations at breakthrough.**

Mineral	Volume fraction (%)	Surface area (m^2/m^3)
Quartz	19	10730
Albite	14	7920
Microcline	15	8480
Phlogopite	09	5100
Muscovite	22	12420
Clinozoisite	0.25	141
Montmorillonite	0.16	90
Clinochlore	0.08	45
Porosity	20.5	-

CONCLUSIONS

Reactive transport modeling of the core infiltration experiment has been able to reproduce the main experimental observations. The modeling results confirm that the dissolution of primary minerals is kinetically controlled. The model made use of rate laws based on published experimental results for the primary minerals, and larger rates for the secondary minerals (simulating conditions close to local equilibrium for these secondary phases). In order to obtain a reasonable agreement between model and experimental results, reactive surface areas between 1 and 2 orders of magnitude smaller than those measured by BET had to be used.

Albite and microcline are the most reactive primary minerals. They dissolve always under far-from-equilibrium conditions. Quartz and muscovite also dissolve, but the magnitudes of the rates are much smaller. Phlogopite undergoes very little reaction. A well defined secondary mineral zonation (C-S-H large Ca/Si, C-S-H small Ca/Si, C-A-S-H, zeolites) develops along the fracture and also through time. Only small amounts of secondary minerals are formed, which is in agreement with experimental observations.

The initial peak in Si and Al concentrations at breakthrough is caused by the dissolution of fines (fine-grained albite in the model). The surface area of these fines dominates the initial total surface area of the fault gouge. Ca is displaced from the exchange sites by K and Na, which are therefore retarded. However, the arrival of the Ca concentration front is also retarded by precipitation of secondary phases (C-S-H) and uptake at surface complexation sites. The increase in Si concentration at later stages of the experiment is caused by the increasing residence time of the solution in the core (decreasing flow velocity; constant primary-mineral dissolution rates), which cannot be balanced by the precipitation of secondary phases. The arrival of the high-pH front is also retarded by surface processes (modeled as Ca^{2+} - H^+ exchange on surface complexation sites). It should be mentioned, though, that retardation caused by these surface sorption processes (surface complexation, cation exchange) has an effect only during the very early evolution of the system (days); long-term behavior is not affected by these processes. The rock does not really have any significant high-pH-buffering capacity.

The results of a limited sensitivity analysis have also shown that solution chemistry is not greatly affected by i) not including zeolites as potential secondary minerals, ii) not including prehnite as an analogue of a C-A-S-H phase (a Ca-zeolite precipitates, instead), or iii) including trace primary minerals in the model. The effect of not including crystalline C-S-H phases in the model is more substantial. Cementitious C-S-H phases (Ca/Si < 1.67) are predicted to precipitate, but Si concentrations in solution are somewhat overestimated.

An important finding from this core infiltration experiment was that the interaction between the hyperalkaline solution and the fault zone in the granite caused a significant reduction in the hydraulic conductivity of the rock core, even though the amount of mineral alteration was minor. This reduction in hydraulic conductivity would be beneficial for the performance of a repository. The same trend was observed in the in-situ experiment at the Grimsel Test Site after 3 years of continuous injection of high-pH fluid (Mäder et al., 2006). The fact that the decrease in permeability was significant despite the minor changes in mineralogy, suggests that permeability may be controlled by changes in the structure of the fault gouge (pore geometries) rather than by only the bulk volumetric (porosity) changes.

ACKNOWLEDGMENTS

Funding from Posiva (Finland), discussions with the numerous participants in the HPF and LCS projects, and the detailed comments on the manuscript by Carl Steefel and Wilfried Pfingsten are gratefully acknowledged.

REFERENCES

Berner, U.R., 1988. Modelling the incongruent dissolution of hydrated cement minerals. Radiochimica Acta, 44/45, 387-393.

Berner, U.R., 1992. Evolution of pore water chemistry during degradation of cement in a radioactive waste repository environment. Waste Management, 12, 201-219.

Bossart, P., Mazurek, M., 1991. Structural Geology and Water Flow-Paths in the Migrations Shear Zone. Wettingen (Switzerland), Nagra Technical Report, 91-12.

Bradbury, M.H., Baeyens, B., Geckeis, H., Rabung, Th., 2005. Sorption of Eu(III)/Cm(III) on Ca-montmorillonite and Na-illite. Part 2: Surface complexation modelling. Geochimica et Cosmochimica Acta, 69, 5403-5412.

Eikenberg, J., Hoehn, E., Fierz, T., Frick, U., 1994. Grimsel test site: Preparation and performance of migration experiments with radio-isotopes of sodium, strontium and iodine. Paul Scherrer Institut report, Villigen (Switzerland), Nationale Genossenschaft für die Lagerung radioaktiver Abfälle, Nagra Technical Report, 94-11, 71pp.

Kulik, D.A., Kersten, M., 2001. Aqueous solubility diagrams for cementitious waste stabilization systems: II, end-member stoichiometries of ideal calcium silicate hydrate solid solutions. Journal of the American Ceramic Society, 84, 3017-3026.

Mäder, U.K., Ekberg, Ch., 2006. GTS-HPF Project: Geochemical Evolution of Porewater in the Granitic Shear Zone AU-126 during 3 Years of Interaction with a Hyperalkaline Fluid, and its Interpretation. Wettingen (Switzerland), Nagra Technical Report, 06-08, 133pp.

Mäder, U.K., Fierz, Th., Frieg, B., Eikenberg, J., Rüthi, M., Albinsson, Y., Möri, A., Ekberg, S., Stille P., 2006. Interaction of hyperalkaline fluid with fractured rock: Field and laboratory experiments of the HPF project (Grimsel Test Site, Switzerland). Journal of Geochemical Exploration, 90, 68-94.

Marty, N., Burnol, A., Gaucher, E.C., 2009. Influence of Dissolution/Precipitation Kinetics on the Porosity Clogging Effect during Cement/Clay Interaction. Orléans (France), Bureau de Recherches Géologiques et Minières, Report-56236-FR, 120pp.

Mazurek, M., 2003. Mineralogal - Geochemical Characterisation of the Shear Zone at AU 126m in Support of the HPF Experiment. Wettingen (Switzerland), Unpublished Nagra Internal Report NIB, 03-16, 28pp.

Pfingsten, W., Paris, B., Soler, J.M., Mäder, U.K., 2005. Tracer and reactive transport modelling of the interaction between high-pH fluid and fractured rock: Field and laboratory experiments. Journal of Geochemical Exploration, 90, 95-113.

Rochelle, C.A., Noy, D.J., 2000. GTS/HPF: Mineral Reaction Kinetics under Alkaline Conditions - Review of Literature for Selected Materials. Wettingen (Switzerland), Nagra Internal Report, Unpublished, NIB 00-28, 28pp.

Soler, J.M., Mäder, U.K., 2005. Interaction between hyperalkaline fluids and rocks hosting repositories for radioactive waste: Reactive transport simulations. Nuclear Science and Engineering, 151, 128-133.

Soler, J.M., Mäder, U.K., 2007. Mineralogical alteration and associated permeability changes induced by a high-pH plume: Modeling of a granite core infiltration experiment. Applied Geochemistry, 22, 17-29.

Soler, J.M., Pfingsten, W., Paris, B., Mäder, U.K., Frieg, B., Neall, F., Källvenius, G., Yui, M., Yoshida, P., Shi, P., Rochelle, C.A., Noy, D.J., 2006. Grimsel Test Site - Investigation Phase V. HPF-Experiment: Modelling report. Wettingen (Switzerland), Nagra Technical Report NTB, 05-01, 176pp.

Steefel, C.I., 2008. CrunchFlow. Software for Modeling Multicomponent Reactive Flow and Transport. User's Manual. Earth Sciences Division, Berkeley (USA), Lawrence Berkeley National Laboratory, 90pp.

Wolery, T.J., Jackson, K.J., Bourcier, W.L., Bruton, C.J., Viani, B.E., Knauss, K.G., Delany, J.M., 1990. Current status of the EQ3/6 software package for geochemical modeling. In: Melchior, C., Bassett, R.L. (eds.). Chemical Modeling of Aqueous Systems II. ACS Symposium Series, 416, 104-116.

Manuscript received July 2009;
revision accepted December 2009;
published Online May 2010.